



Li, X., Harkness, P., Worrall, K., Timoney, R., and Lucas, M. (2017) A parametric study for the design of an optimized ultrasonic-percussive planetary drill tool. IEEE Transactions on Ultrasonics, Ferroelectrics, and Frequency Control, 64(3), pp. 577-589.

There may be differences between this version and the published version. You are advised to consult the publisher's version if you wish to cite from it.

<http://eprints.gla.ac.uk/131822/>

Deposited on: 25 November 2016

Enlighten – Research publications by members of the University of Glasgow
<http://eprints.gla.ac.uk>

A parametric study for the design of an optimized ultrasonic-percussive planetary drill tool

Xuan Li*, Patrick Harkness*, Kevin Worrall*, Ryan Timoney*, and Margaret Lucas*

*School of Engineering, University of Glasgow, Glasgow, G12 8QQ, UK

Abstract—Traditional rotary drilling for planetary rock sampling, in-situ analysis and sample return, is challenging because the axial force and holding torque requirements are not necessarily compatible with lightweight spacecraft architectures in low-gravity environments. This article seeks to optimize an ultrasonic-percussive drill tool to achieve rock penetration with lower reacted force requirements, with a strategic view towards building an Ultrasonic Planetary Core Drill (UPCD) device. The UPCD is a descendant of the Ultrasonic/Sonic Driller/Corer (USDC) technique. In these concepts, a transducer and horn (typically resonant at around 20kHz) is used to excite a toroidal free-mass which oscillates chaotically between the horn tip and drill base at lower frequencies (generally between 10Hz to 1kHz). This creates a series of stress pulses which are transferred through the drill-bit to the rock surface and, while the stress at the drill-bit tip/rock interface exceeds the compressive strength of the rock, cause fractures that result in fragmentation of the rock. This facilitates augering and downward progress. In order to ensure that the drill-bit tip delivers the greatest effective impulse (the time-integral of the drill-bit tip/rock pressure curve exceeding the strength of the rock), parameters such as the spring rates and the mass of the free-mass, drill-bit and transducer have been varied and compared in both computer simulation and in practical experiment. The most interesting findings, and those of particular relevance to deep drilling, indicate that increasing the mass of the drill-bit has a limited (or even positive) influence on the rate of effective impulse delivered.

Index Terms—Ultrasonic drilling, percussive drilling, dynamic modelling, planetary sample retrieval

I. INTRODUCTION

RELIABLE and effective tools to collect rock samples, conduct in-situ analysis and deliver sample-return missions in lower gravity fields need to be developed as the conventional drilling technique is often associated with high axial forces, high holding torques and high power consumption [1]. A potential alternative is to use an ultrasonic transducer and horn to superimpose vibrations onto the cutting motion [2] in the longitudinal direction. However, it is still a challenge whether this technique is feasible to be employed for planetary rock drilling. Operating at 20kHz, there is perhaps insufficient time between percussion impact events for the drill-bit to release a considerable amount of energy to fracture the rock.

This project has received funding from the European Union's Seventh Framework Programme for research, technological development and demonstration under Grant Agreement No. 607015. Corresponding author: Dr. Patrick Harkness (email: Patrick.Harkness@glasgow.ac.uk Tel: (+44)(0)141 330 3233)

To tackle this problem, the Ultrasonic/Sonic Driller/Corer (USDC) was prototyped and is described in [3]. The USDC is driven by a piezoelectric Langevin-style transducer which operates at around 20kHz. This vibration is amplified by a resonant step horn [4] and then used to excite a percussive stack which consists of a free-mass and a drill-bit.

The free-mass oscillates between tens of Hz to about 1000Hz [5]. The energy of multiple ultrasonic vibration cycles is thus accumulated and transferred to the free-mass and hence to the drill-bit/rock interface when an impact occurs [6]. The rate of progress is broadly proportional to the rate at which effective impulse is delivered, where this rate is equal to the growth of the bit/rock contact-pressure time integral exceeding the compressive strength of the rock [4].

The UPCD is based on a multi-parameter optimization (parameters which include compression spring rates, free-mass, drill mass, transducer mass, internal pre-load and external weight-on-bit) of this fundamental architecture, with respect to the rate of effective impulse, using a UPCD assembly as shown in Fig. 1. The ultrasonic transducer is a Sonic Systems L500 device powered by a P100 control unit. The device is a half-wavelength system with piezoceramic rings located near the nodal point and a radiating face vibration displacement that can be adjusted between 2 to 12 microns peak-to-peak depending on the input power. The step horn attached to the transducer has a theoretical gain of eight, amplifying this amplitude. The piezoceramic rings in the transducer can be operated across a wide range of temperatures, depending on the piezoceramic rings selected [1].

The UPCD has three spiral compression springs on the longitudinal rails, opposed by a single wave spring located around the drill-bit, as shown in Fig. 1, which together allow longitudinal motions of the transducer and horn. The toroidal free-mass at the tip of the horn sits within a six-keyed spline shaft, contiguous with the lance, which is used to mate with and deliver impulse to the drill-bit. The spline shaft, and hence the lance, is rotated by a spline bush within a cog gear seated on an angular contact bearing and rotated by a pinion attached to a Maxon DC motor. This permits rotation of the lance for the drill string assembly [7] and ensures that the teeth of the drill-bit impact different regions of the rock as drilling progresses. This ensures that the contact area remains small, the interface pressures remain correspondingly high, and the rate of progress is sufficiently rapid for planetary drilling [8].

The rear springs absorb the shock associated with impacts of the free-mass, minimizing the loads transmitted to the drill

deployer. The front spring, meanwhile, also applies a static internal pre-load on the dynamic stack that returns the drill string to the free-mass [9] during zero weight-on-bit testing. Operationally, the front spring is also involved in separating the bayonet-style connections envisaged for drill string itself [7].

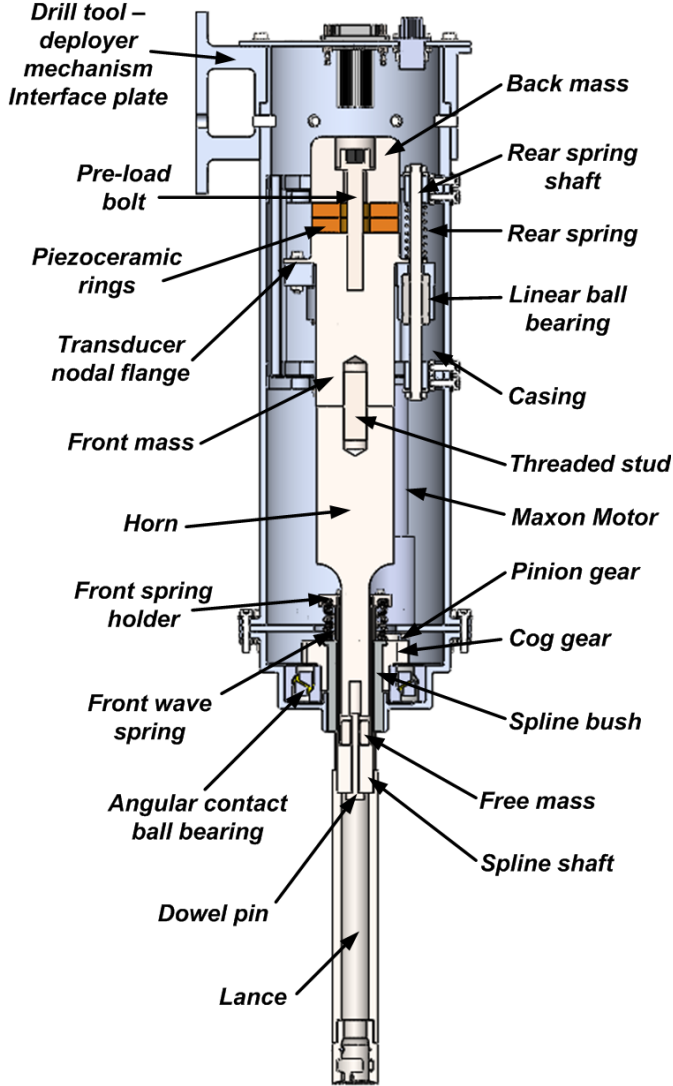


Fig. 1. Cross-sectional view of the full wavelength drill tool

It has been found in both simulation and experiment that specific combinations of compression spring rates, operating at different internal pre-loads and weights-on-bit, can cause the dynamic force generated in the springs to reach zero, so that there is a temporary separation with the result that the casing and the springs rattle. A significant weight-on-bit and a stiff front spring are likely to cause more separation of the front spring and casing. However, from a mechanical standpoint, rattling is not a major problem so long as the front spring is designed to remain aligned and captive.

II. UNLOADED TRANSDUCER AND HORN MODEL

There are three interfaces in the drill tool, which are horn/free-mass, free-mass/drill-bit and drill-bit/rock interactions. In order to analyze the dynamic behavior of these

interactions, a simple and reliable transducer and horn model needs first to be established as the basis of a full model of the UPCD, and which can be readily validated by experimental ultrasonic vibration measurements of the actual transducer and horn.

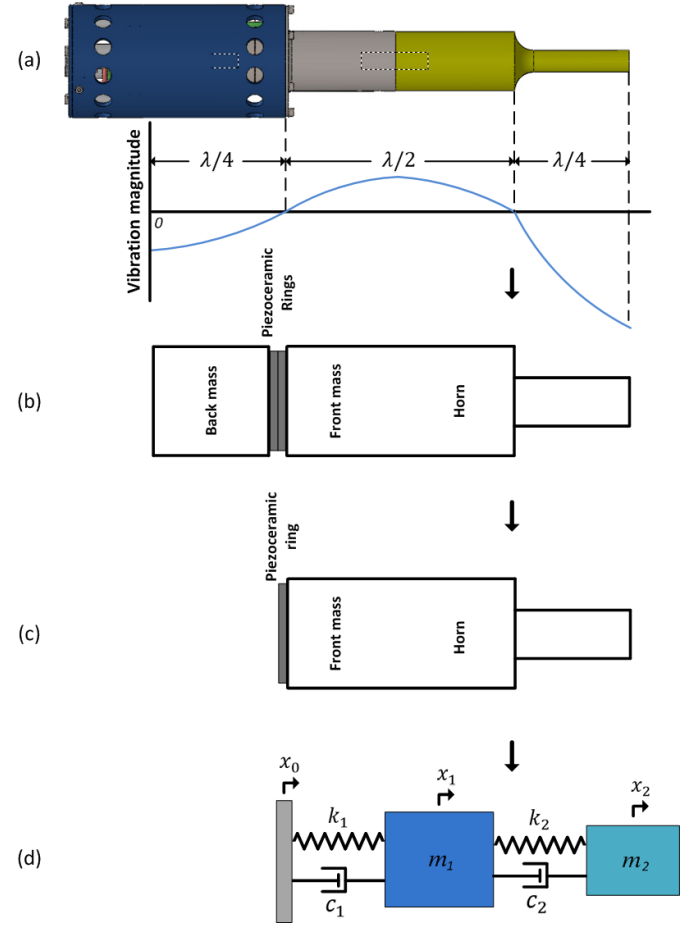


Fig. 2. Full wavelength transducer and horn structure and simplification: (a) transducer and horn and waveform at resonance, (b) transducer and horn structure, (c) simplification, (d) a 2-DOF vibrating system

Fig. 2 illustrates the structure of proposed full wavelength transducer and horn model as a mass-spring-damper system.

Fig. 2 (a) shows a typical vibration displacement amplitude profile, where the length of both the back mass (hidden in blue casing) and front mass of the transducer are each a quarter-wavelength of the ultrasonic wave in the transducer's titanium alloy Grade 5 Ti-6Al-4V body. A half-wavelength resonator (or horn) with a tapered-step diameter reduction at its mid-point, is connected to the transducer's radiating face via a threaded stud. As a result, the overall ultrasonic stack has two nodal points when operating in its full-wavelength longitudinal mode: one near the piezoceramic rings in the transducer and one near the step in the horn. Fig. 2 (b) illustrates the basic structure of this transducer and horn. The back mass is removed in Fig. 2 (c), reducing the structure to a simplified two degree-of-freedom (DOF), one-dimensional model, shown in Fig. 2 (d), to represent the transducer and horn as a mass-spring-damper model.

Compared to previous models of USDC/UPCD style devices

(including the work in [4], [6] and [10]) which compute the effective horn mass and then attribute the rest of the material to the transducer mass, this current work proposes an integrated modelling technique to represent the transducer and horn itself. This is important because the input signal is an AC voltage to the piezoceramic rings (which generates the modelled mechanical vibrations) and the output signals are then the piezoceramic ring vibrations, transducer radiating face vibrations and horn tip vibrations. In addition the control system, which adjusts the supplied voltage to the piezoceramic rings to compensate for the energy transfer due to the impacts of drilling, can now be modelled as part of an integrated system, which yields a more representative model of the device.

The 2-DOF model has two eigen-frequencies. The 1st frequency corresponds to the masses vibrating in-phase, and the 2nd frequency corresponds to anti-phase movement representing the operational mode of vibration. x_0 is the absolute displacement of the piezoceramic ring, x_1 represents the absolute displacement in the middle of the basal part of the horn at the location of the anti-node of the operating mode, and x_2 is the absolute displacement at the tip of the horn. m_1 and m_2 are the effective masses which represent the amount of material that is participating in the acoustic energy transfer, k_1 and k_2 are the modelled internal stiffnesses, and c_1 and c_2 are the corresponding damping coefficients.

Taking the transducer and horn dimensions and experimental measurements into account, the parameters of the transducer and horn now can be identified. The method used here strictly follows the procedure presented in [11], pages 53-59.

A. 2-stage transducer and horn model

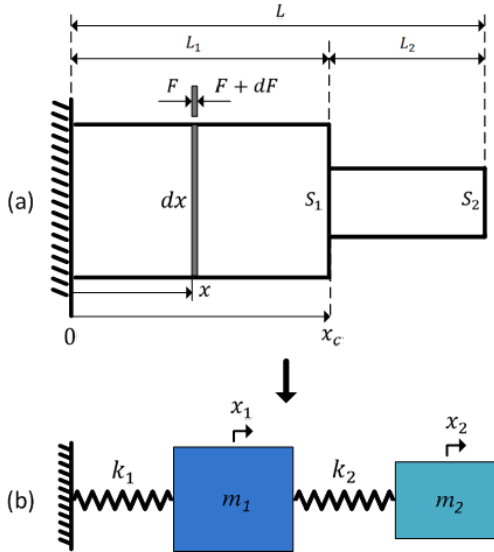


Fig. 3. (a) Simplified 2-stage transducer-horn distributed parameter model, (b) 2-DOF lumped parameter model

The transducer and horn used in this study is a two-stage bar, with different cross-sectional areas as shown in Fig. 3. x_c is the coordinate at the step, L_1 and L_2 are the lengths of each stage, S_1 and S_2 represent the cross-sectional areas, and L is the overall length. Because the piezoceramic ring is sited near the nodal point, it may be temporarily removed and the left end can

be modelled as a rigid boundary.

In order to obtain the longitudinal wave dynamic equations, a thin arbitrary section of length dx at coordinate x has been defined. F is the force generated at coordinate x and the value is increased by dF over the section length. Therefore, the dynamic equation can be written as:

$$\rho \frac{\partial^2 D_i(x, t)}{\partial t^2} = E \frac{\partial^2 D_i(x, t)}{\partial x^2} \quad (1)$$

where ρ is the density of the bar, E is the Young's modulus, $D_i(x, t)$ is the displacement at coordinate x at time t , and $i = 1, 2$ (for the two stages). Assuming the bar vibrates harmonically, the displacement of the arbitrary section dx has an expression $D(x, t) = D(x) \sin(\omega t)$. Therefore equation (1) can be re-written as:

$$\frac{d^2 D_i(x)}{dx^2} + \frac{\rho \omega^2}{E} D_i(x) = 0 \quad (2)$$

The general solutions to the bar's dynamic differential equation (2) are:

$$D_i(x) = \begin{cases} A_1 \sin(kx) + A_2 \cos(kx) & 0 < x < x_c \\ B_1 \sin(kx) + B_2 \cos(kx) & x_c < x < L \end{cases} \quad (3)$$

where $k = \sqrt{\frac{\rho \omega^2}{E}}$ that represents the wavenumber of the longitudinal vibration, ω is the natural frequency of the bar. Since the transducer and horn is fixed at the left end, and the right end is freely vibrating, the boundary conditions of the bar can be defined as:

$$\begin{aligned} D_1(x, t)|_{x=0} &= 0 \\ \frac{dD_2(x, t)}{dx} \Big|_{x=L} &= 0 \end{aligned} \quad (4)$$

Substituting the boundary conditions (4) into equation (3) gives:

$$D_i(x) = \begin{cases} A \sin(kx) & 0 < x < x_c \\ B \cos[k(x - L)] & x_c < x < L \end{cases} \quad (5)$$

where $A = A_1$, $B = \frac{B_1}{\sin(kL)}$. Furthermore, at the point x_c , there is a continuity of displacement for the two stages and the forces are equal and opposite at the connection. Hence, the following equations can be derived:

$$\begin{aligned} D_1(x, t)|_{x=x_c} &= D_2(x, t)|_{x=x_c} \\ \frac{\partial D_2(x, t)}{\partial x} \Big|_{x=x_c} &= \frac{S_1}{S_2} \frac{\partial D_1(x, t)}{\partial x} \Big|_{x=x_c} \end{aligned} \quad (6)$$

Implementing equation (6) into equation (5) gives:

$$\begin{aligned} A \sin(kx_c) &= B \cos[k(x_c - L)] \\ A S_1 \cos(kx_c) &= -B S_2 \sin[k(x_c - L)] \end{aligned} \quad (7)$$

After a re-arrangement of equation (7), it gives an expression of the distributed parameter model of the 2-stage transducer and horn:

$$\tan(kx_c) \tan[k(x_c - L)] = -\frac{S_1}{S_2} \quad (8)$$

As discussed, a 2-DOF model, as shown in Fig. 3 (b) can replace the 2-stage transducer and horn for simulation purposes. However, the 2-DOF model excludes the damper sets to facilitate calculation of the stiffness and mass using the eigenvalue-eigenvector method [11].

According to the Euler-Lagrange equations [12] and assumption of the 2-DOF system's harmonic longitudinal vibration ($x_1 = V_1 \sin(\omega t)$, $x_2 = V_2 \sin(\omega t)$), the following dynamic equations for the 2-DOF system can be written:

$$\begin{aligned} (k_1 + k_2 - m_1 \omega^2) V_1 - k_2 V_2 &= 0 \\ -k_2 V_1 + (k_2 - m_2 \omega^2) V_2 &= 0 \end{aligned} \quad (9)$$

where V_1 and V_2 are the vibration amplitudes of the two effective masses. The ω values are the eigenvalues of the distributed parameter model calculated in equation (8). The eigenvectors are the amplitude ratios between the 1st and 2nd stages of the 2-stage transducer and horn as measured experimentally at resonances.

An additional condition to identify the stiffness and effective mass of the 2-DOF system is the conservation of energy. It is assumed that the total energy of the distributed parameter model is completely conserved through the 2-DOF model which gives the following equation:

$$\begin{aligned} \frac{E}{2} \left[S_1 \int_0^{x_c} \left(\frac{dD_1(x)}{dx} \right)^2 dx + S_2 \int_{x_c}^L \left(\frac{dD_2(x)}{dx} \right)^2 dx \right] \\ = \frac{1}{2} k_1 V_1^2 + \frac{1}{2} k_2 (V_2 - V_1)^2 \end{aligned} \quad (10)$$

The dimensions and material parameters of the 2-stage transducer and horn are given in TABLE I. The wavelength for a metal bar with a non-uniform cross-sectional area, representing the transducer and horn shown in Fig. 2 (a), has been calculated from following equation (11) [13], [14]:

$$\lambda = \frac{1}{2\pi f} \sqrt{\frac{E}{\rho}} \sqrt{(2\pi)^2 + (\ln n)^2} \approx 0.2655\text{m} \quad (11)$$

where λ is the wavelength, f is the natural frequency of the bar, $\sqrt{\frac{E}{\rho}}$ is the speed of the stress wave in the material, and n is the ratio of the horn cross-sectional areas $\frac{S_1}{S_2}$.

TABLE I
DIMENSIONS AND MATERIAL PROPERTIES OF THE TRANSDUCER AND HORN

1 st Stage Radius (R_1)	0.017m
2 nd Stage Radius (R_2)	0.00625m
1 st Stage Length (L_1)	0.132m
2 nd Stage Length (L_2)	0.0625m
Young's Modulus (E)	$1.14 \times 10^{11} \text{N/m}^2$
Density (ρ)	4439kg/m^3

B. Piezoelectric model

The Sonic Systems L500 transducer uses Navy type III PZT-8 piezoceramic rings, suitable for high power applications with low a loss factor [15]. The interaction between the

electrical and mechanical aspects of the piezoelectric behaviors can be described by the following relationships:

$$\begin{aligned} \varepsilon &= s^E \sigma + d \mathbb{E} \\ \mathbb{D} &= d \sigma + \varepsilon^T \mathbb{E} \\ \mathbb{E} &= -\mathbb{g} \sigma + \frac{\mathbb{D}}{\varepsilon^T} \\ \varepsilon &= s^D \sigma + \mathbb{g} \mathbb{D} \\ d &= \varepsilon^r \varepsilon^0 \mathbb{g} \end{aligned} \quad (12)$$

where ε is the strain, σ is applied stress, s^E is the elastic compliance at constant electric field, d is the piezoelectric charge constant, \mathbb{D} is the dielectric displacement, \mathbb{E} is the electric field strength, ε^T is the permittivity under constant stress, \mathbb{g} is the voltage constant, s^D is the elastic compliance with an open electrode circuit, and ε^0 is the permittivity of free space which is $8.85 \times 10^{-12} \text{F/m}$. Taking into account the relationships $\sigma = \frac{F_0}{S_0}$, $\mathbb{E} = \frac{U}{l_0}$ and $\mathbb{D} = \frac{q}{S_0}$, equation (13) can be derived.

$$\begin{aligned} x_0 &= \frac{s_{33}^E l_0}{S_0} F_0 + d_{33} u \\ q &= d_{33} F_0 + \frac{\varepsilon_{33}^T S_0}{l_0} u \end{aligned} \quad (13)$$

These parameters for the piezoceramic rings were obtained from the supplier (Morgan Electro Ceramics) [15]. Here, S_0 is the area, l_0 is the thickness, F_0 is the applied force, u is the supplied voltage, q is the stored electrical charge. The parameters that are specified for the 33 polarization direction are: s_{33}^E , the elastic compliance for stress, d_{33} , the charge constant and ε_{33}^T , the permittivity.

The properties and coefficients used in the model are shown in TABLE II, where these parameters are substituted into equation (13) for the purposes of numerical simulation.

TABLE II
PZT-8 RINGS PROPERTIES AND COEFFICIENTS

Piezoceramic ring type PZT-8	
Outer Diameter (OD)	0.038m
Inner Diameter (ID)	0.013m
Area (S_0)	$1 \times 10^{-3} \text{m}^2$
Thickness (l_0)	0.0065m
Elastic Compliance (s_{33}^E)	$13.5 \times 10^{-12} \text{m}^2/\text{N}$
Charge Constant (d_{33})	$225 \times 10^{-12} \text{C/N}$
Permittivity (ε_{33}^T)	$8.85 \times 10^{-9} \text{F/m}$

C. Transducer and horn model

Using the transducer and horn described in section A and the piezoelectric properties described in section B in section II, the 2-DOF model has been developed into a complete transducer and horn model. According to the Euler-Lagrange equations [12], the dynamic equations of the transducer and horn can be written as:

$$\begin{aligned} m_1 \ddot{x}_1 + k_1 (x_1 - x_0) + c_1 (\dot{x}_1 - \dot{x}_0) + k_2 (x_1 - x_2) + c_2 (\dot{x}_1 - \dot{x}_2) &= 0 \\ m_2 \ddot{x}_2 - k_2 (x_1 - x_2) - c_2 (\dot{x}_1 - \dot{x}_2) &= 0 \end{aligned} \quad (14)$$

The interaction force F_0 between the piezoceramic ring and the 2-DOF model can be extracted as:

$$F_0 = k_1(x_1 - x_0) + c_1(\dot{x}_1 - \dot{x}_0) \quad (15)$$

The coefficients c_1 and c_2 can be adjusted to tune the simulated ultrasonic vibrations x_1 and x_2 to match experimental measurements. For this purpose, the supplied AC voltage in experiments was measured by a GE 8115 differential probe at the piezoceramic rings to determine a relationship with horn displacement.

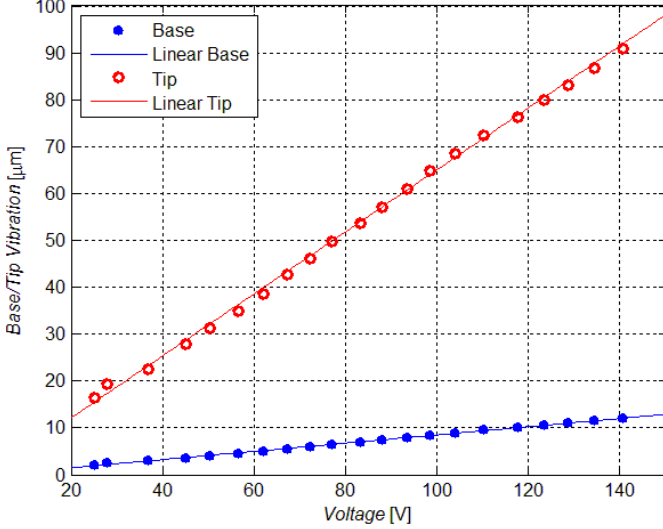


Fig. 4. Supplied voltage vs base/tip vibrations of the transducer and horn

Fig. 4 shows a linear relationship between the supplied voltage and the transducer and horn vibration displacement amplitudes as the transducer radiating face vibration increases from $2.0\mu\text{m}$ to $12\mu\text{m}$ (as controlled by the P100 generator). The horn tip vibrations were captured using a 1-D laser vibrometer (Polytec OFV 303 sensor head interfaced with an OFV3001 vibrometer controller).

As stated in [16], for the horn ratio of base diameter to tip diameter, the amplitude gain can be calculated from the parameters in TABLE I to be 7.42. As a verification, the gain of the tapered horn in the experiment can be calculated from Fig. 4 as 7.72, a close agreement with the theoretical prediction.

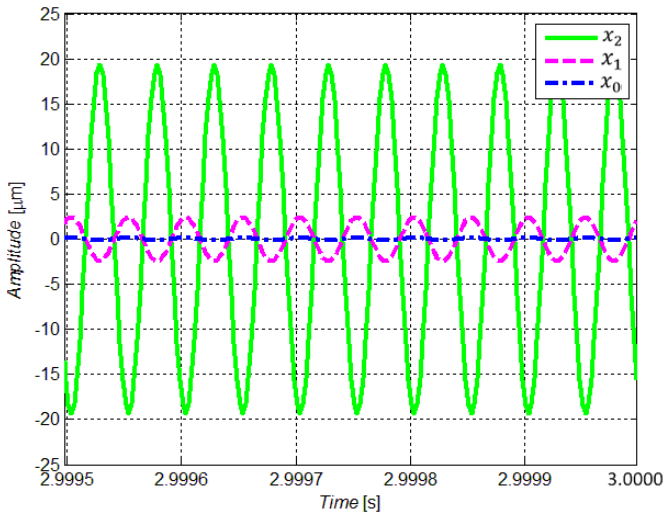


Fig. 5. Steady-state vibrations of piezoceramic ring x_0 , 1st mass x_1 and 2nd mass x_2 of the transducer and horn

In the following experiments, the transducer excitation displacement is selected to be $5\mu\text{m}$ peak-to-peak which develops a $38.6\mu\text{m}$ peak-to-peak horn tip vibration. The driving voltage is around 62V peak-to-peak from Fig. 4. Using the information of the input voltage and output vibration displacements from the transducer and horn in experiments, the transducer and horn model can be implemented to estimate damping coefficients by tuning the model to fit the experimentally measured displacements.

Simulated results of the unloaded transducer and horn are illustrated in Fig. 5. Both x_1 and x_2 are consistent with the experimental measurements shown in Fig. 4 and the anti-phase characteristic between x_1 and x_2 is also consistent with experimental observation. The resonant frequency of the transducer and horn model has only a 0.1% difference from the distributed parameter model of the 2-stage transducer and horn.

Therefore, the reliability and accuracy of the transducer and horn model is confirmed, which allows us to proceed to calculate the dynamic behavior of the drilling tool during interaction with the free-mass, drill-bit and impact plate.

III. ULTRASONIC PLANETARY CORE DRILL (UPCD) MODEL

Numerical model and dynamic differential equations of the rest of the dynamic stack are derived for integration with the transducer and horn model according to spring-mass-damper interactions set out in Fig. 6. Subsequently, a negative feedback control system is designed which simulates the functions of the P100 control unit in maintaining the ultrasonic vibrations at a desired level by varying the supplied voltage in response to variations in the applied weight-on-bit.

Parameters including front and rear spring rates, masses of free-mass, drill-bit mass and transducer mass are examined using the model to maximize the rate of effective impulse transferred to the target material. The simulated results are then validated through experiments.

As can be seen, the transducer is supported by the rear compression spring, k_r . A mass m_{fm} with a contact spring rate k_{fm} and a damping coefficient c_{fm} models the free-mass, sitting between the horn tip and the drill-bit. Finally, a drill-bit mass m_{dr} is placed between the free-mass and the front compression spring, k_f . The contact stiffness of the drill-bit is k_{dr} and damping coefficient is c_{dr} .

Three free-masses (of mass 5g, 6g and 7g) are used to examine their effect on the rate of the effective impulse. More significantly, the drill-bit mass will change in service (as the drill extends) and so three drill-bit masses (of mass 80g, 160g and 240g) are examined, and finally the effect of transducer mass will be explored at 1.925kg, with additional dummy masses being used to reach to a 2.925kg and 3.925kg. Experimental tests are then carried out with the drill-bit in contact with a tool steel impact plate represented in simulations by a Kelvin-Voigt model [17], which represents the rock for validation of the model.

Equation (16) shows the dynamic characteristics of the drill tool percussive process. For the transducer and horn, they will exhibit ultrasonic vibrations (around 20kHz) superimposed

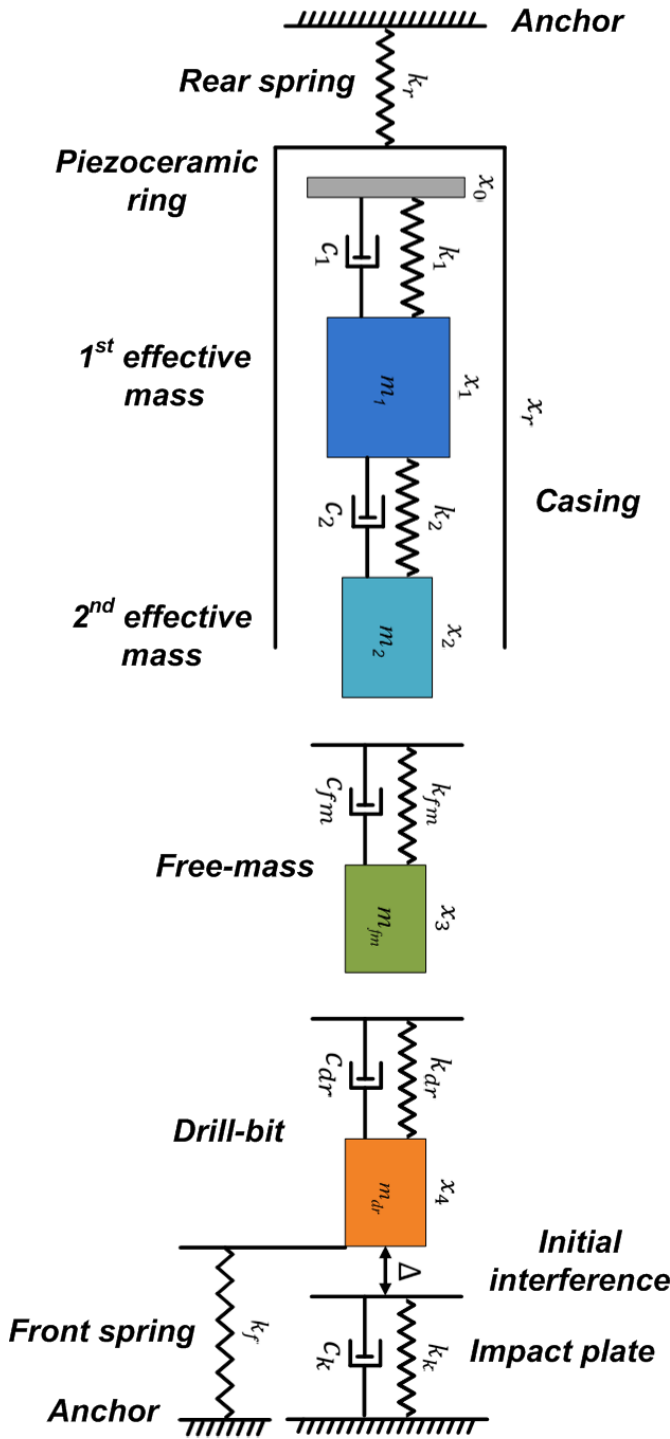


Fig. 6. Mass-Spring-Damper model of the UPCD assembly

with apparently chaotic motions at sonic frequencies. In order to obtain the apparently chaotic behaviors, the casing's absolute displacement has been defined as x_r . m_{dm} represents the summation of the material mass of the transducer and horn and casing, but subtracts the effective mass of the transducer and horn, m_1 and m_2 . The subscript of m_{dm} means 'dead mass', whose motion is affected by the rear spring k_r but does not participate directly in the ultrasonic motion. F_r means the dynamic force in the rear spring during percussion. F_{sr} is the

static pre-load of the rear spring before percussion is activated. This value is prescribed in both simulation and experiments.

$$m_{dm}\ddot{x}_r - F_0 - F_r = 0$$

$$F_r = F_{sr} - k_r x_r$$

$$m_1\ddot{x}_1 + k_1(x_1 - x_0) + c_1(\dot{x}_1 - \dot{x}_0) + k_2(x_1 - x_2) + c_2(\dot{x}_1 - \dot{x}_2) = 0$$

$$m_2\ddot{x}_2 - k_2(x_1 - x_2) - c_2(\dot{x}_1 - \dot{x}_2) + k_{fm}(x_2 - x_3) + c_{fm}(\dot{x}_2 - \dot{x}_3) = 0$$

$$m_{fm}\ddot{x}_3 - k_{fm}(x_2 - x_3) - c_{fm}(\dot{x}_2 - \dot{x}_3) + k_{dr}(x_3 - x_4) + c_{dr}(\dot{x}_3 - \dot{x}_4) = 0$$

$$m_{dr}\ddot{x}_4 - k_{dr}(x_3 - x_4) - c_{dr}(\dot{x}_3 - \dot{x}_4) + k_k x + c_k \dot{x} + F_f = 0$$

$$F_f = F_{sf} - k_f x$$

$$\begin{cases} x = x_4 - \Delta, & \Delta > 0 \\ x = x_4, & \Delta \leq 0 \end{cases} \quad (16)$$

x_3 and x_4 are the absolute displacements of the free-mass and drill-bit. F_{sf} is the static pre-load in the front spring before percussion is triggered, which has the same value as F_{sr} because, for the experimental configuration, the drill tool is operated in horizontal direction. F_f is the dynamic force in the front spring during percussion and x is the relative displacement between drill-bit and target surface. Δ is the initial interference/gap between the drill-bit and the steel impact plate.

IV. AMPLITUDE CONTROL SYSTEM DESIGN

As high frequency vibrations are converted to low frequency apparently chaotic behaviors, during the drill tool hammering against the rock, the ultrasonic amplitude will drop if a constant voltage is supplied to the piezoceramic rings. Consequently, the P100 control unit (from Sonic Systems Ltd., Ilminster, UK) locks the phase between current and voltage to the piezoceramic rings and compensates power during drilling [18], in order to ensure ultrasonic amplitude remains steady.

The control system assumes that R_d represents the desired root mean square (rms) ultrasonic vibration amplitude, U is the control voltage amplitude for the unloaded transducer and horn, R_i is the rms ultrasonic vibration amplitude of the current control cycle, and U_{i+1} is the control voltage amplitude to be established. G is a gain value that must be estimated, but the overall vibration control algorithm can still be established:

$$\begin{cases} U_{i+1} = \frac{GUR_d}{R_i}, & R_d > R_i \\ U_{i+1} = \frac{UR_d}{GR_i}, & R_d \leq R_i \end{cases} \quad (17)$$

Due to percussion-induced waveform distortion, it is difficult to estimate the change in the AC signals level. As a result, the rms values of each ultrasonic vibration cycle are evaluated.

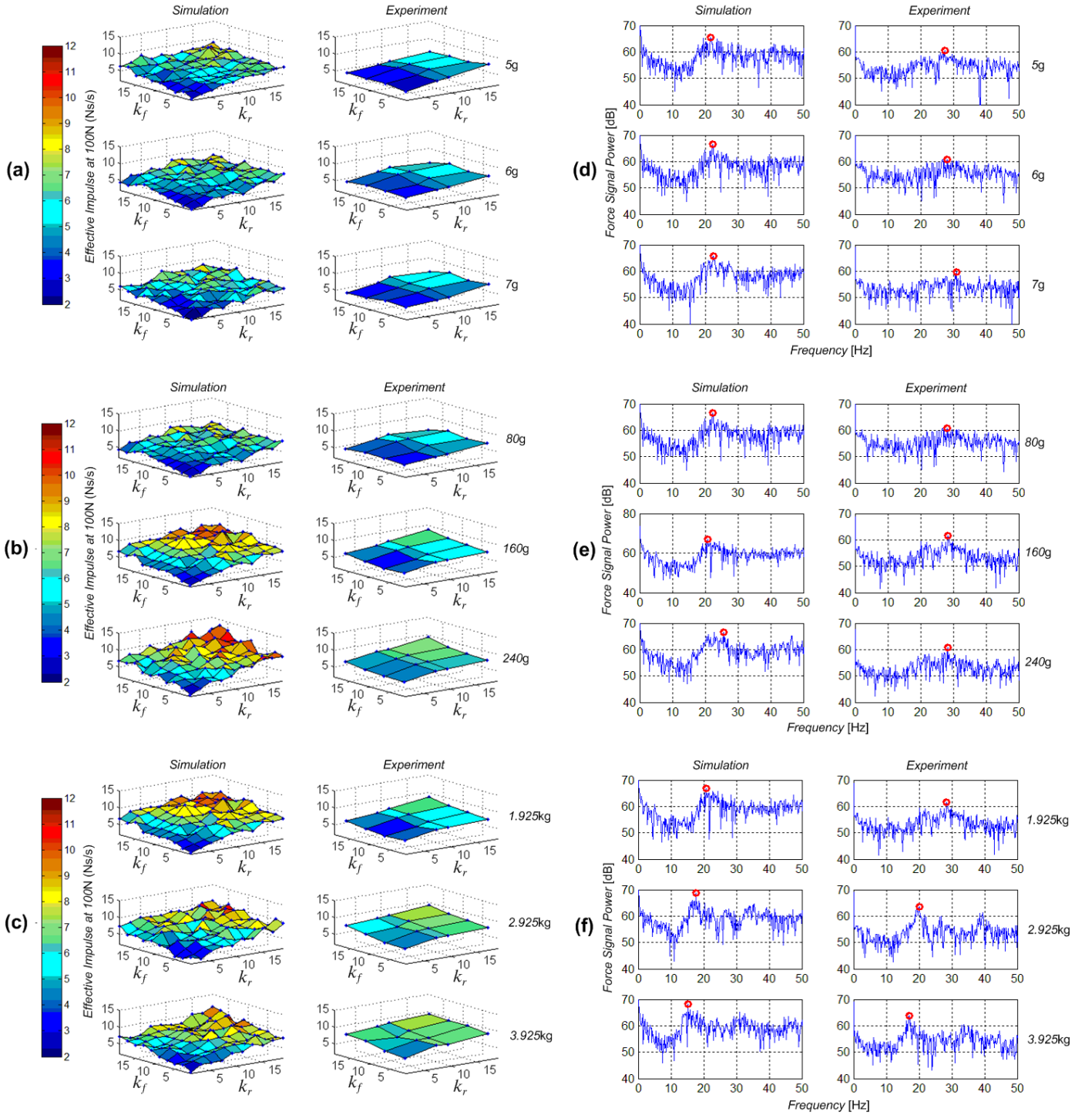


Fig. 7. Predicted and measured effective impulse delivered above 100N threshold during change in (a) free-mass mass 5g, 6g and 7g, (b) drill-bit mass 80g, 160g and 240g, (c) transducer mass 1.925kg, 2.925kg and 3.925kg, and the percussion force frequency response with a front spring rate 5N/mm and a rear spring rate 10N/mm during change in (d) free-mass mass, (e) drill-bit mass and (f) transducer mass

V. PARAMETRIC OPTIMIZATION OF THE DYNAMIC STACK

The dynamic stack is optimized with an aim of maximizing the rate of effective impulse to the impact surface. The parameters investigated are the masses of free-mass, drill-bit, and transducer, as well as the compression spring rates.

For the unloaded transducer and horn model, m_1 , k_1 , c_1 , m_2 , k_2 and c_2 have been identified in section II. However, for the stiffness of free-mass, k_{fm} , and drill-bit, k_{dr} , estimation is

difficult due to the apparently chaotic motions and changes in contact time during collisions. Nonetheless, there are a number of research papers dedicated to the study of collisions between two or multiple moving objects and as the collisions between horn tip, free-mass and drill-bit have been simplified as a mass-spring-damper model, the calculation of the contact stiffness of each object can follow the formula that is described in [19]. For instance, for the free-mass contact stiffness k_{fm} calculation:

$$k_{fm} = \frac{m_{fm}}{(1 + \mu)T_c^2} (\pi^2 + (\ln(e))^2) \quad (18)$$

where μ is the mass ratio of two objects in collision, in this case $\mu = \frac{m_{fm}}{m_2}$, T_c is the duration of collision, and e is the coefficient of the restitution of collision.

As can be seen in equation (18), the stiffness is dominated by the contact time of collision but mass ratio is also an important factor. Therefore, for each free-mass examined, there should be a slight difference in stiffness values, but here this is regarded as insignificant. The contact stiffness of the impact plate (representing rock for model validation purposes), meanwhile, is tuned to exhibit a close match between the (peak) simulated force and the (peak) experimentally recorded force.

TABLE III
PARAMETERS OF THE DYNAMIC STACK

1 st effective mass (m_1)	0.183kg
Spring rate of m_1 (k_1)	6.48×10^8 N/m
Damping of m_1 (c_1)	0.05Ns/m
2 nd effective mass (m_2)	0.018kg
Spring rate of m_2 (k_2)	2.57×10^8 N/m
Damping of m_2 (c_2)	0.173Ns/m
Spring rate of m_{fm} (k_{fm})	2.71×10^8 N/m
Damping of m_{fm} (c_{fm})	0Ns/m
Spring rate of m_{dr} (k_{dr})	3.25×10^8 N/m
Damping of m_{dr} (c_{dr})	0Ns/m
Spring rate of impact plate (k_k)	9×10^6 N/m
Damping of impact plate (c_k)	18Ns/m
Initial interference (Δ)	0m

The identified parameters of the dynamic stack are shown in TABLE III for a 5g free-mass, an 80g drill-bit and a 1.925kg transducer. The contact time of collision between the horn tip and free-mass has been estimated in [4] using finite element analysis, estimating a contact time of 1.2×10^{-5} seconds. As the free-mass and drill-bit have the same material properties as the horn, the contact time for the free-mass and drill-bit is also assumed to be 1.2×10^{-5} seconds. Calibration studies have shown that even if the contact time is doubled or halved, the delivered rate of effective impulse varies by less than 2%.

The coefficient of the restitution e during collision for titanium on titanium is assumed to be 1 (purely elastic) between the mechanical parts in the simulation model.

In running the models, an internal pre-load of 10N is applied prior to percussion, and both spring rates are changed as $k_f, k_r \in [1 - 19]$ N/mm with an increment of 2N/mm. In comparison, available springs in experiments are limited to k_f values of [5, 10.05, 14.95, 19.9] N/mm for the front springs and for the rear springs k_r values of [3.84, 10, 12.24, 19.98] N/mm.

We recall that pulverization of rock is caused by the stress exceeding the compressive strength of the material. Therefore, a 100N force threshold has been prescribed to represent a medium-soft rock compressive limit of 100MPa under a 1mm² cutting area. The impulse delivery rate above this threshold is the key dependent variable illustrated in Fig. 7. It should be mentioned that a single drill-bit of 80g and a transducer self-weight of 1.925kg was used during the study of changing the mass of the free-mass Fig. 7 (a). For changing the mass of the drill-bit, Fig. 7 (b), a 6g free-mass and transducer self-weight of 1.925kg was employed. A 6g free-mass and a

160g drill-bit were adopted to examine the effect on the rate of delivered impulse during the change of the transducer mass, Fig. 7 (c).

Fig. 7 (a), (b) and (c) illustrate that the rate of effective impulse generally increases with both k_f and k_r . There is also an improvement as the drill-bit mass rises from 80g to 240g, both in simulation and in experiment, which is encouraging when considering the need to build longer and heavier drill strings, but there are limited effects due to the change in the masses of free-mass and transducer across the ranges considered. Fig. 7 (d), (e) and (f), meanwhile, show the frequency spectra of the impact force signals, based on a fixed front spring rate of 5N/mm and rear springs rate of 10N/mm. These present a different pattern, as summarized in TABLE IV. Given that small displacements in the rig can strongly affect the weight-on-bit values, some systematic error is found, but the trends appear consistent.

TABLE IV
FREQUENCY PEAKS OF SIMULATION AND EXPERIMENT

Percussion force frequency (Hz)			
Free-Mass	5g	6g	7g
Simulation	21.57	22.33	22.52
Experiment	27.47	28.04	30.90
Drill Mass	80g	160g	240g
Simulation	22.33	20.80	25.58
Experiment	28.04	28.42	28.23
Transducer Mass	1.925kg	2.925kg	3.925kg
Simulation	20.80	17.75	15.27
Experiment	28.42	20.03	16.98

VI. MOTIONS WITHIN THE DYNAMIC STACK

Thus far, all our results have been calculated from the time domain percussion force signals. However, the numerical predictions of the physical motions of the transducer and horn, free-mass and drill-bit must be compared to the experimental behaviors. Experimental validations are carried out for the drill operating both in free-air (a large positive value of Δ , without an applied load) and in contact with a target (a zero value of Δ , with an applied load).

Fig. 8 illustrates the experimental setup of the test rig. (a) shows a 3-D model, and (b) is a photograph of the experimental rig, showing the additional masses used to modify the drill-bit mass and transducer mass. The mass of the free-mass is modified by a simple exchange from the free-mass holder. At the tip of the drill-bit, an impact plate made of tool steel is attached to a force sensor (Kistler 9321B), which backs onto a heavy stanchion. The whole assembly can be driven by a DC voltage controlled linear actuator (LT225-1-300P) in order to vary the weight-on-bit and emulate the motion control system [20]. The linear actuator is demobilized in this study.

During operation, a 3-D laser vibrometer (Polytec CLV3000) is used to measure the velocity of the horn tip, free-mass and drill-bit, a differential probe (GE 8115) is used to record the high frequency AC supplied voltage into the piezoceramic rings, and a data acquisition unit (PicoScope 4424) is employed to record the data.

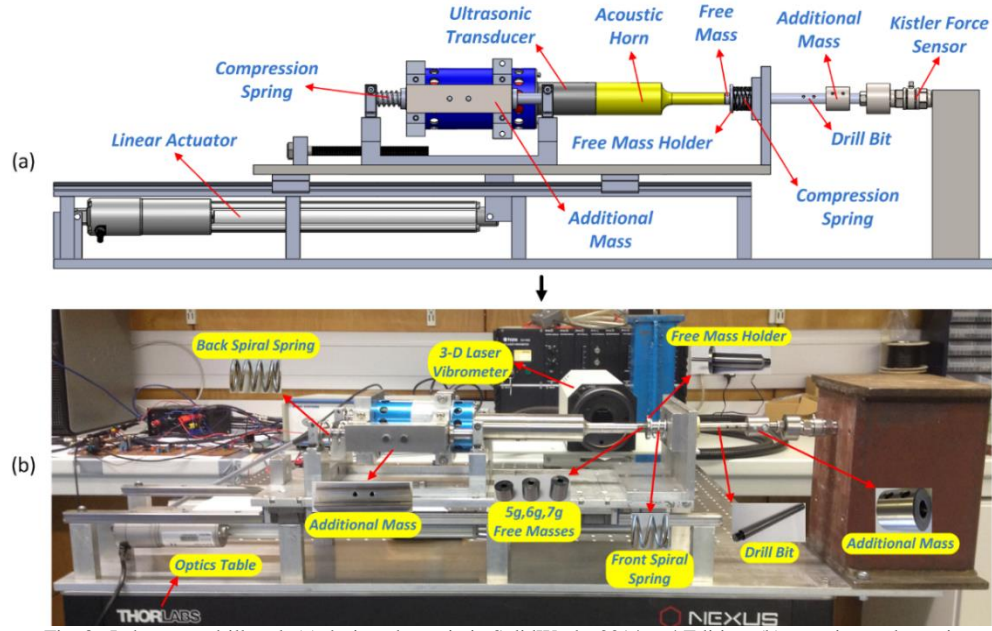


Fig. 8. Laboratory drill tool: (a) designed test rig in SolidWorks 2014 x64 Edition, (b) experimental test rig

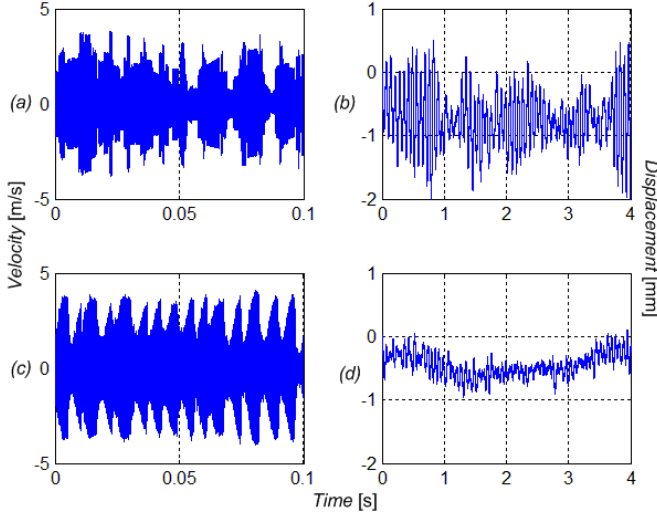


Fig. 9. Simulated and recorded velocities and displacements of the horn tip: (a) simulated velocity, (b) simulated displacement, (c) measured velocity, (d) measured displacement

In this study, a 5g toroidal free-mass is used, along with a single drill-bit of 80g, a front spring rate of 10.05N/mm, rear springs rate of 10N/mm, a 10N internal pre-load and a 5 μ m peak-to-peak transducer radiating face vibration magnitude. The parameters of the dynamic stack are shown in TABLE III.

A. Drill tool percussion in free-air

Fig. 9 shows the simulated and experimental velocities and calculated displacements for the horn tip during percussion in free-air (no external applied load).

The simulated and measured horn tip velocities both present peaks of ± 4 m/s. Both velocity-time graphs show the control system restoring amplitude after each impact with free-mass, and allow a first estimate of the free-mass oscillation frequency (125Hz-250Hz) to be made. In terms of the position of the horn tip, the simulated results show a range of -2mm to +0.3mm due to collisions with the free-mass.

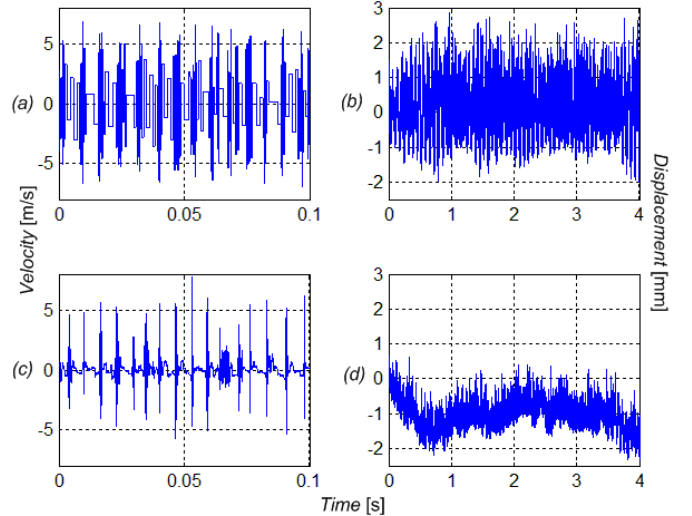


Fig. 10. Simulated and recorded velocities and displacements of the free-mass: (a) simulated velocity, (b) simulated displacement, (c) measured velocity, (d) measured displacement

Experimentally, a range of -1mm to +0.2mm is calculated based on the laser vibrometer's output. An estimated frequency range (10Hz-25Hz) may also be made which represents the solid body mode of the transducer and horn.

Fig. 10 presents the simulated and measured free-mass velocities and displacements.

The free-mass velocities, which are crucial to the performance and life of the drill, are within a -6m/s to +6m/s range. Despite the apparently chaotic characteristics of the velocity response, the gross behavior of the velocity traces does appear to contain consistent 125Hz-250Hz oscillation. The simulated results estimate a displacement range of -2mm to +2.5mm while, experimentally, a range of -2mm to +0.5mm is measured.

Fig. 11 exhibits the simulated and measured velocities and displacements of the drill-bit.

The simulated and experimental velocity graphs for both exhibit impact velocities of approximately 1.5m/s. As

previously, the frequency can be estimated: the drill-bit percussion (into free-air) is at around 100Hz-300Hz. The simulated displacement is about -1.5mm to +3mm and the experimental data lies in the -1.2mm to +1.6mm range.

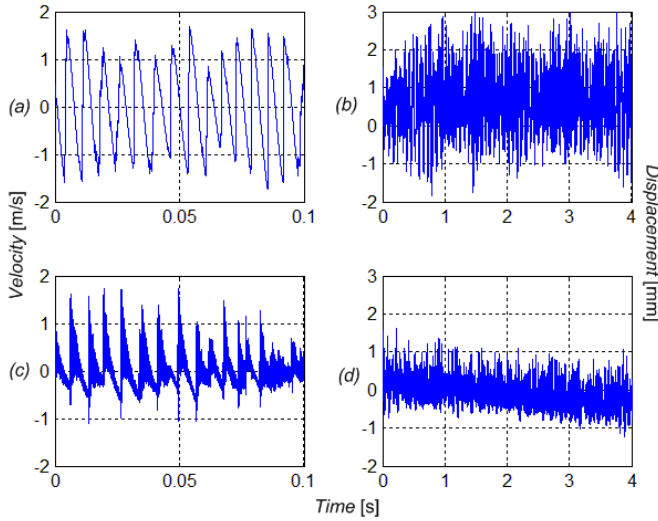


Fig. 11. Simulated and recorded velocities and displacements of the drill-bit: (a) simulated velocity, (b) simulated displacement, (c) measured velocity, (d) measured displacement

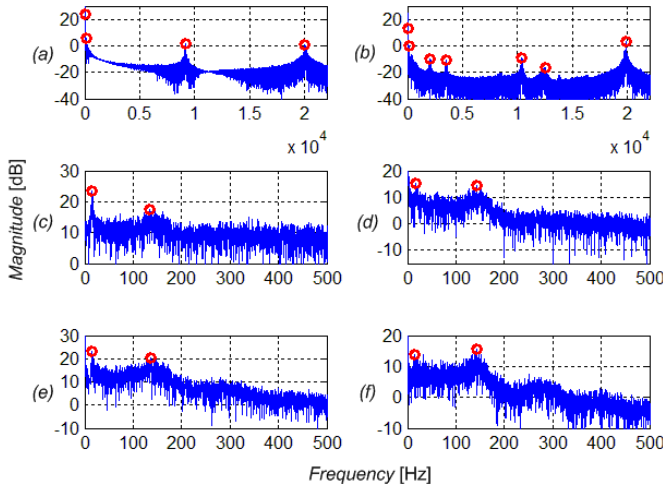


Fig. 12. Spectra of simulated and measured displacements: (a) simulated horn tip, (b) measured horn tip, (c) simulated free-mass, (d) measured free-mass, (e) simulated drill-bit, (f) measured drill-bit

In order to improve on the frequency accuracy estimated from the previous three figures, their displacements frequency spectra are presented in Fig. 12. Peaks are highlighted in red circles and TABLE V is created accordingly.

TABLE V
FREQUENCY PEAKS OF SIMULATION AND EXPERIMENT

Part	Simulated resonant frequency (Hz)			
Horn Tip	14.7	136.7	9120	20010
Free-Mass	14.7	133.8	-	-
Drill-Bit	14.7	136.5	-	-
Part	Measured resonant frequency (Hz)			
Horn Tip	15.8	139	10400	19840
Free-Mass	16.6	143.8	-	-
Drill-Bit	13.7	142.1	-	-

The dominant behaviors are clearly at around 15Hz (transducer and horn solid body motion) and 140Hz (free-mass

and drill-bit percussion). Other peaks are associated with the ultrasonic vibration, its harmonics, and other bending and torsional modes.

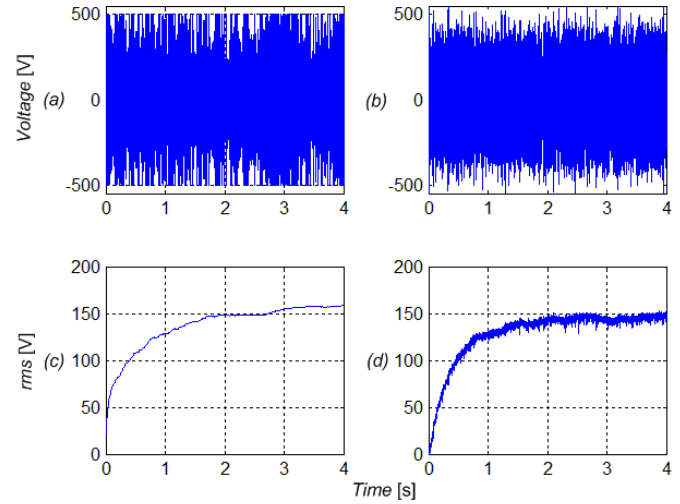


Fig. 13. Simulated and measured voltage to piezoceramic rings: (a) simulated AC voltage, (b) measured AC voltage, (c) simulated rms voltage, (d) measured rms voltage

Turning to the electrical behavior, Fig. 13 illustrates the voltage across the piezoceramic rings estimated from the simulation and measured using a differential probe. Both graphs show the alternating voltage signal of -500V to +500V, with the rms voltages climbing to approximately 150V as the drill system stabilizes in the first two seconds of operation.

Note that these figures show a start-up transient, while the previous figures have been taken from the steady-state behaviors. A saturation function is introduced in the simulation to limit the level of supplied voltage to the piezoceramic rings, in order to be consistent with experimental measurements.

B. Drill tool percussion against a steel impact plate

The simulations and experiments reported in section A in section VI were repeated, but for percussion against a steel impact plate (with an external applied load).

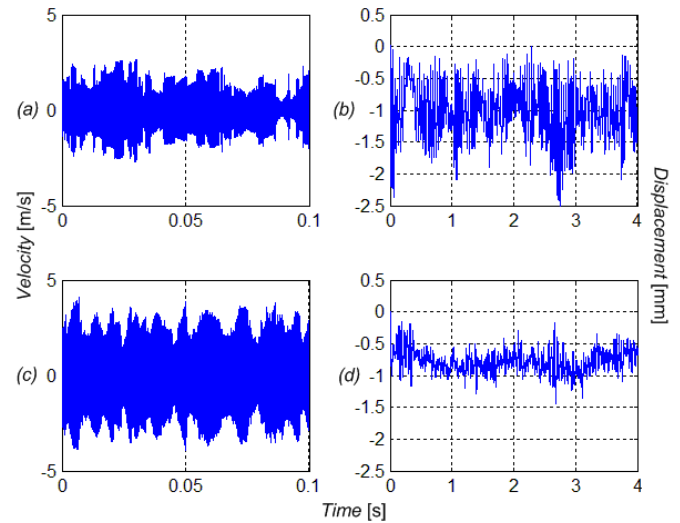


Fig. 14. Simulated and measured velocities and displacements of the horn tip: (a) simulated velocity, (b) simulated displacement, (c) measured velocity, (d) measured displacement

The simulated and measured velocities and displacements of the horn tip are presented in Fig. 14. The velocity of the horn tip during percussion is estimated to be $\pm 2.5\text{m/s}$ from the simulation, which is slightly lower than the measured velocity of $\pm 3.2\text{m/s}$. In both cases, the velocity is lower than for the drill tool percussion in free-air, but both graphs still exhibit the restoration of velocity after each impact with free-mass. The free-mass oscillation frequency is still estimated from the graphs to be in the range of 125Hz-250Hz. The displacement of the horn tip shows a reasonably good agreement between simulation and experiment, with ranges of -2mm to 0mm and -1.5mm to 0mm. An estimate of the transducer and horn solid body motion frequency from these results is 20Hz-30Hz, a little higher than for the percussion in free-air case.

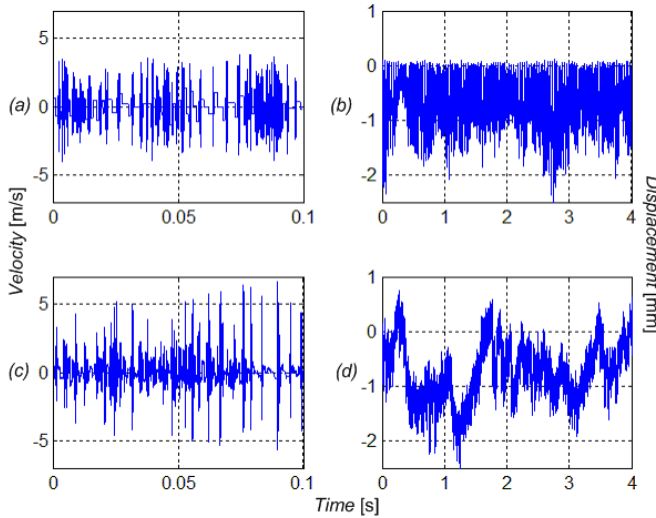


Fig. 15. Simulated and measured velocities and displacements of the free-mass: (a) simulated velocity, (b) simulated displacement, (c) measured velocity, (d) measured displacement

Fig. 15 presents the simulated and measured free-mass velocities and displacements for percussion against a steel impact plate.

In this case, the free-mass velocity has dropped to a -5m/s to +5m/s range. The oscillation frequency estimated from the graphs is slightly higher, at approximately 150Hz-300Hz. With regards to the calculated displacements, the results of both the simulation and experiment are consistently in the -2.5mm to 0.8mm range.

The predicted and measured velocities and displacements of the drill-bit are shown in Fig. 16. Both simulated and measured velocities present an impact value of around 1m/s, which is lower than seen during percussion in free-air, and the frequency is higher at around 200Hz-400Hz. With regards to the displacement, the simulation value ranges from -1.5mm to around +0.2mm. In contrast, the measurement value ranges from -0.7mm to +0.3mm. The causes to this mismatch are the noisy velocity signals of the experimental measurement, which gives rise to different values in displacement during integration, and friction between mechanical parts.

Once again, the estimated frequency analysis carried out on the previous three figures may be improved by calculating the associated spectra, shown in Fig. 17. Peaks are highlighted in red, from which TABLE VI is created. In comparison with the drill tool percussion in free-air case, Fig. 12, the peaks in Fig.

17 seem less prominent due to the introduction of a steel impact plate which is affecting the behaviour of the component. However, the trend can still be identified.

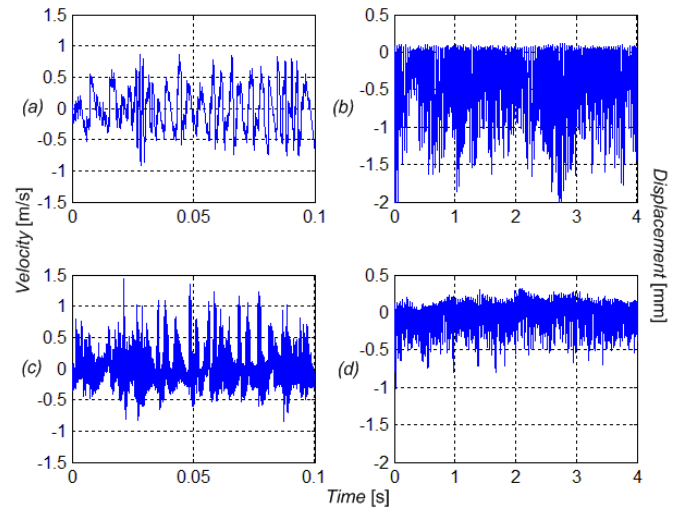


Fig. 16. Simulated and measured velocities and displacements of the drill-bit: (a) simulated velocity, (b) simulated displacement, (c) measured velocity, (d) measured displacement

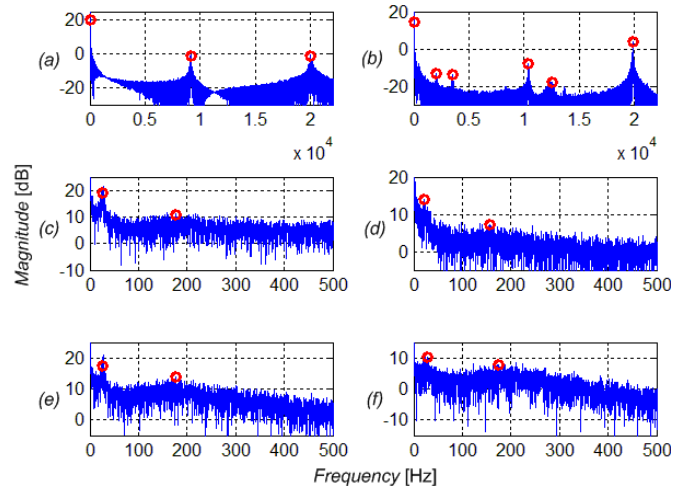


Fig. 17. Spectra of simulated and measured displacements: (a) simulated horn tip, (b) measured horn tip, (c) simulated free-mass, (d) measured free-mass, (e) simulated drill-bit, (f) measured drill-bit

TABLE VI
FREQUENCY PEAKS OF SIMULATION AND EXPERIMENT

Part	Simulated resonant frequency (Hz)			
	26.9	-	9129	20010
Horn Tip	26.9	-	-	-
Free-Mass	26.9	177.7	-	-
Drill-Bit	26.9	177.3	-	-
Part	Measured resonant frequency (Hz)			
	22.5	-	10400	19850
Horn Tip	22.1	157.2	-	-
Free-Mass	27.9	175.5	-	-
Drill-Bit				

The transducer and horn solid body mode, that is superimposed on the ultrasonic motion, and the motions of all other parts of the drill stack, increase in frequency during percussion against a steel impact plate (the transducer and horn solid-body movement now exceeds 25Hz). However, the peaks are less prominent than in Fig. 12, especially for the displacements spectrum of the free-mass and drill-bit where, instead, apparently chaotic motions predominate.

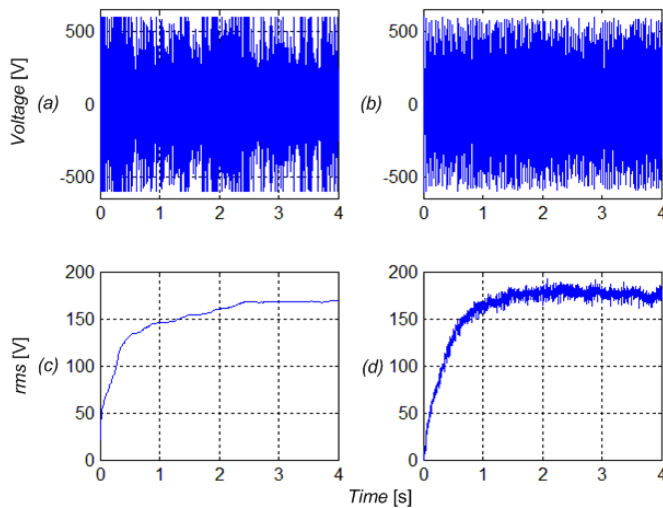


Fig. 18. Simulated and measured supplied voltage to piezoceramic rings: (a) simulated AC voltage, (b) measured AC voltage, (c) simulated rms voltage, (d) measured rms voltage

The electrical behavior, as shown in Fig. 18, illustrates that the system stabilizes over a few seconds, as before. However, due to energy being transferred into the steel impact plate during percussion, the steady-state rms voltage is now closer to 180V. Again, in order to be consistent with the measured supplied voltage to the piezoceramic rings, a saturation function is used in the simulation to limit the voltage levels.

C. Investigation of change in pre-load

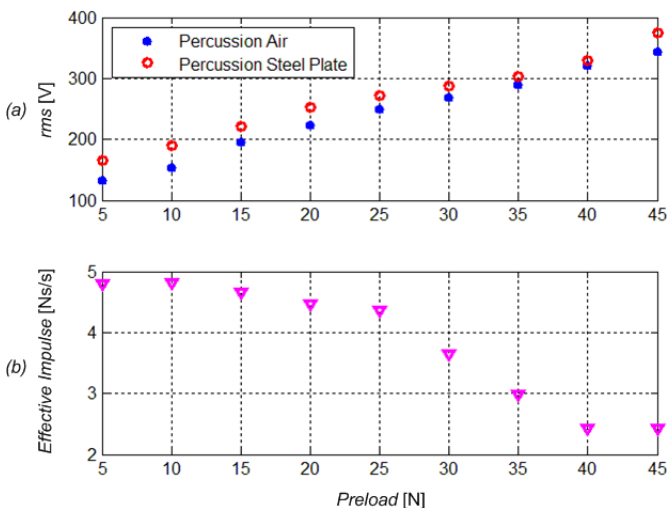


Fig. 19. Supplied voltage rms and rate of effective impulse delivered above 100N threshold during change of pre-load in springs: (a) voltage rms, (b) rate of effective impulse

Throughout this study, the internal pre-load (the compression force between the springs) has been set at around 10N to suppress springs rattling. By varying the pre-load in experiments, it is possible to compare the demand on voltage for percussion in free-air and hammering against a steel impact plate. It is apparent that a greater pre-load increases the required voltage, which is used to overcome a higher dynamic force in the springs during percussion. Furthermore, for pre-load values higher than about 25N, there is a significant reduction in the rate of the effective impulse delivery.

VII. CONCLUSION

This paper presents the results of an integrated electrical/mechanical model of an ultrasonic-percussive stack, which has been used to obtain some overall design rules (such as the advantage of stiffer internal springs under light pre-load).

In the parameters space considered, free-masses ranging from 5g to 7g perform equally well in the delivered effective impulse. A drill-bit mass increasing from 80g to 240g hardly affects the delivered effective impulse, showing a slight ascending trend which is encouraging for deeper drilling applications necessitating multiple drillstring sections. A drop in the solid body motion frequency is observed for an increase in the transducer mass. However, the effective impulse is slightly increased, due to a higher percussion force generated against the steel impact plate. Nonetheless, a significant increase in the assembly mass is generally undesirable as it dissatisfies the lighter mass and lower power budget requirements for space missions.

From the investigation of the applied pre-load, experiments suggest that the value should not exceed 25N because of the increase in power consumption, decrease in the effective impulse delivered, and increase in the pressure between horn tip, free-mass and drill-bit, which is likely to accelerate wear and damage of parts and deteriorate the percussion performance.

REFERENCES

- [1] Y. Bar-Cohen, S. Sherrit, B. P. Dolgin, X. Bao, Z. Chang, S. Dharmendra, R. Krahe, J. Kroh, S. Du, and T. Peterson, "Ultrasonic/sonic drilling/coring (USDC) for planetary applications," in *Proceedings of SPIE's 8th Annual International Symposium on Smart Structures and Materials*, no. 4327, pp. 5-8, 2001.
- [2] V. I. Babitsky, V. K. Astashev, and A. Meadows, "Vibration excitation and energy transfer during ultrasonically assisted drilling," *Journal of Sound and Vibration*, vol. 308, no. 3-5, pp. 805-814, Dec. 2007.
- [3] S. Sherrit, B. P. Dolgin, Y. Bar-Cohen, D. Pal, J. Kroh, and T. Peterson, "Modeling of Horns for Sonic/Ultrasonic Applications," *IEEE Ultrasonics Symposium*, 1999.
- [4] P. Harkness, M. Lucas and A. Cardoni, "Maximization of the Effective Impulse Delivered by a High-Frequency/Low-Frequency Planetary Drill Tool," *IEEE Transactions on Ultrasonics, Ferroelectrics, and Frequency Control*, vol. 58, no. 11, Nov. 2011.
- [5] Z. Chang, S. Sherrit, X. Bao, and Y. Bar-Cohen, "Design and analysis of ultrasonic horn for USDC (Ultrasonic/Sonic Driller/Corer)," in *Proceedings of the SPIE Smart Structures Conference, San Diego, CA*, vol. 5388, 2004.
- [6] X. Bao, Y. Bar-Cohen, Z. Chang, B. P. Dolgin, S. Sherrit, D. S. Pal, S. Du, and T. Peterson, "Modeling and computer simulation of ultrasonic/sonic driller/corer (USDC)," *IEEE Transactions of Ultrasonics, Sonics and Frequency Control*, vol. 50, no. 9, pp. 1147-1160, Sep. 2003.
- [7] R. Timoney, P. Harkness, K. Worrall, X. Li, A. Bolhovitins, and M. Lucas, "The Development of the European Ultrasonic Planetary Core Drill (UPCD)," *AIAA Space 2015 Conference and Exposition, Pasadena, CA*, 2015.
- [8] P. Harkness, M. Mcrobb, Y. W. Loh, M. Hyde, and M. Lucas, "A Rock-Coring Campaign in an Analogue Environment," *AIAA Space 2014 Conference and Exposition, San Diego, CA*, 2014.
- [9] Y. Bar-Cohen, S. Sherrit, B. Dolgin, D. Pal, and T. Peterson, "Ultrasonic/sonic drilling/coring (USDC) for in-situ planetary applications," *SPIE Smart Structures Conference, Newport Beach, CA*, no. 3992-101, Mar. 2000.
- [10] C. Potthast, J. Twiefel, and J. Wallaschek, "Modelling approaches for an ultrasonic percussion drill," *Journal of Sound and Vibration*, vol. 308, no. 3-5, pp. 405-417, Dec. 2007.
- [11] X. Li, "Modelling and autoresonant control design of ultrasonically assisted drilling applications," *Loughborough University Institutional*

- Repository, Mechanical, Electrical and Manufacturing Engineering, PhD Theses*. pp. 45-50, 2014.
- [12] T. Bruce, "Energy Methods," ISBN 0-03, *Advanced Dynamics for Engineers, HRW Series in Mechanical Engineering*. United States of America: CBS College Publishing, 1984.
 - [13] H. Hocheng and K. L. Kuo, "On-line tool wear monitoring during ultrasonic machining using tool resonance frequency," *Journal of Materials Processing Technology*, vol. 123, pp. 80-84, 2002.
 - [14] L. Stanasel and F. Ardelean, "The parameter design of the ultrasonic exponential horns," *Nonconventional Technologies Review*, no. 4, pp. 54-58, 2010.
 - [15] "Piezoelectric Ceramics," *MorganElectroCeramics*.
<http://www.morganelectroceramics.com/resources/literature/>.
 - [16] S. Sherrit, S. A. Askins, M. Gradziol, B. P. Dolgin, X. Bao, Z. Chang, and Y. Bar-Cohen, "Novel Horn Designs for Ultrasonic/Sonic Cleaning Welding, Soldering, Cutting and Drilling," in *Proceedings of the SPIE Smart Structures Conference, San Diego, CA*, vol. 4701, no. 34, 2002.
 - [17] V. P. Madan, "On Longitudinal Vibrations of a Semi-Infinite Voigt-Kelvin Rod with Non-Uniform Viscoelastic Properties," *Journal of Mathematical Analysis and Applications*, vol. 28, pp. 88-92, 1969.
 - [18] V. I. Babitsky, A. N. Kalashnikov, and F. V. Molodtsov, "Autoresonant control of ultrasonically assisted cutting," *Mechatronics*, vol. 14, no. 1, pp. 91-114, Feb. 2004.
 - [19] K. Li and A. P. Darby, "Modelling a buffered impact damper system using a spring-damper model of impact," *Structure Control and Health Monitoring*, vol. 16, pp. 287-302, 2009.
 - [20] X. Li, K. Worrall, P. Harkness, R. Timoney, A. Bolhovitins, and M. Lucas, "A motion control system design for an Ultrasonic Percussive Coring/Drilling (UPCD) unit," *AIAA Space 2015 Conference and Exposition, Pasadena, CA*, 2015.